In vivo non-invasive confocal fluorescence imaging beyond 1,700 nm using superconducting nanowire single-photon detectors

Wang, Feifei; Ren, Fuqiang; Ma, Zhuoran; Qu, Liangqiong; Gourgues, Ronan; Zadeh, Iman Esmaeil; Los, Johannes W.N.; Qin-Dregely, Jessie; Dai, Hongjie; More Authors

DOI
10.1038/s41565-022-01130-3

Publication date
2022

Document Version
Final published version

Published in
Nature Nanotechnology

Citation (APA)
Wang, F., Ren, F., Ma, Z., Qu, L., Gourgues, R., Zadeh, I. E., Los, J. W. N., Qin-Dregely, J., Dai, H., & More Authors (2022). In vivo non-invasive confocal fluorescence imaging beyond 1,700 nm using superconducting nanowire single-photon detectors. *Nature Nanotechnology*, *17*(6), 653-660. https://doi.org/10.1038/s41565-022-01130-3

nature nanotechnology

ARTICLES

https://doi.org/10.1038/s41565-022-01130-3

In vivo non-invasive confocal fluorescence imaging beyond 1,700 nm using superconducting nanowire single-photon detectors

Feifei Wang[1,5], Fuqiang Ren[1,5], Zhuoran Ma[1,5], Liangqiong Qu[2], Ronan Gourgues[3], Chun Xu[1], Ani Baghdasaryan[1], Jiachen Li[1], Iman Esmaeil Zadeh[4], Johannes W. N. Los[3], Andreas Fognini[3], Jessie Qin-Dregely[3] and Hongjie Dai[1] ✉

Light scattering by biological tissues sets a limit to the penetration depth of high-resolution optical microscopy imaging of live mammals in vivo. An effective approach to reduce light scattering and increase imaging depth is to extend the excitation and emission wavelengths to the second near-infrared window (NIR-II) at >1,000 nm, also called the short-wavelength infrared window. Here we show biocompatible core–shell lead sulfide/cadmium sulfide quantum dots emitting at ~1,880 nm and superconducting nanowire single-photon detectors for single-photon detection up to 2,000 nm, enabling a one-photon excitation fluorescence imaging window in the 1,700–2,000 nm (NIR-IIc) range with 1,650 nm excitation—the longest one-photon excitation and emission for in vivo mouse imaging so far. Confocal fluorescence imaging in NIR-IIc reached an imaging depth of ~1,100 μm through an intact mouse head, and enabled non-invasive cellular-resolution imaging in the inguinal lymph nodes of mice without any surgery. We achieve in vivo molecular imaging of high endothelial venules with diameters as small as ~6.6 μm, as well as CD169 + macrophages and CD3 + T cells in the lymph nodes, opening the possibility of non-invasive intravital imaging of immune trafficking in lymph nodes at the single-cell/vessel-level longitudinally.

In vivo high-resolution optical microscopic imaging of mice has empowered investigations into: biological structures; the molecular nature and identity of cell surface receptors; and cellular processes, events and functions at the single-cell level. However, the heterogeneous nature and complex compositions of biological tissues present a major challenge, limiting the imaging penetration and signal to background ratios (SBRs) due to light scattering and endogenous tissue autofluorescence. Extending the excitation wavelength to the near-infrared (NIR) and short-wave infrared (SWIR) (900–3,000 nm) ranges by multiphoton imaging has been highly successful in suppressing scattering and affording greater penetration depths, but still relies on invasive surgery to expose underlying organs such as the brain and lymph nodes to afford sufficient imaging depths and resolution[1–6]. Up to 1,700 nm excitation has been employed by three-photon microscopy[7], enabling >500-μm-deep through-skull (with scalp removed), three-dimensional volumetric imaging of the mouse brain[8].

Various fluorescent/luminescence dyes and nanoparticle probes with emission in the 1,000–1,700 nm range have been developed in recent years, including small organic molecules[9,10], carbon nanotubes[11], quantum dots (QDs)[12,13] and rare-earth nanoparticles[14–16]. When using these dyes and probes, both confocal[12,17] and light-sheet microscopy (LSM)[18,19] (employing one-photon excitation up to 1,540 nm and emission up to 1,700 nm) benefited from reduced scattering of both excitation and emission light[19], affording non-invasive in vivo microscopy of blood microvessels and molecular imaging at the single-cell level. In vivo NIR-II (previously defined in the 1,000-1,700 nm window) microscopy imaging has facilitated investigating mouse models of cardiovascular diseases, brain injury and cancer, as exemplified by imaging of CD4, CD8, OX40 and other biomarkers on immune cells in the tumour microenvironment in response to immunotherapy[12,18–20].

One of the factors that limited the optical imaging depth into biological tissues is water absorption[21]; water exhibits a local peak at ~1,445 nm due to the vibrational overtone mode of O–H bond bending (Fig. 1a and Supplementary Fig. 1). In the 800–1,400 nm range (including the previously defined 1,300–1,400 nm NIR-IIa sub-window)[22], light absorption is relatively low and imaging depths in tissues such as the brain are dominated by scattering (Fig. 1b). It is possible to image at centimetre depth, but there is a loss of resolution due to light scattering (Fig. 1b)[23]. Both water absorption and scattering influence the NIR-IIb sub-window (1,500–1,700 nm)[24] imaging depths in mouse brains, with an effective attenuation length[1] of $l_e = 1/(1/l_s + 1/l_a)$, where l_s is the scattering length in a mouse brain and can be mimicked by 5% intralipid solution[18], and l_a is the attenuation length of light due to water absorption (Fig. 1b). NIR-IIb affords a longer l_e than the 1,000–1,400 nm range due to reduced light scattering (Fig. 1b), allowing for deeper imaging. The 1,700 nm NIR-IIb borderline is set by the upper detection limit of indium gallium arsenide (InGaAs) detectors (900–1,700 nm) commonly used for NIR-II/SWIR imaging. Beyond 1,700 nm, light scattering is further reduced but water adsorption increases (Fig. 1a,b). Here we define the NIR-IIc sub-window as 1,700–2,000 nm and revised the NIR-II window to 1,000–3,000 nm (with the upper bound being the same as SWIR[25]). The final NIR-II/SWIR sub-window for one-photon excitation imaging is ~2,100–2,300 nm (defined here as NIR-IId), which has a similar attenuation length to NIR-IIc (Fig. 1b) and beyond which

---

[1]Department of Chemistry and Bio-X, Stanford University, Stanford, CA, USA. [2]School of Medicine, Stanford University, Stanford, CA, USA. [3]Single Quantum B.V., Delft, the Netherlands. [4]Department of Imaging Physics, Delft University of Technology, Delft, the Netherlands. [5]These authors contributed equally: Feifei Wang, Fuqiang Ren, Zhuoran Ma. ✉e-mail: hdai@stanford.edu

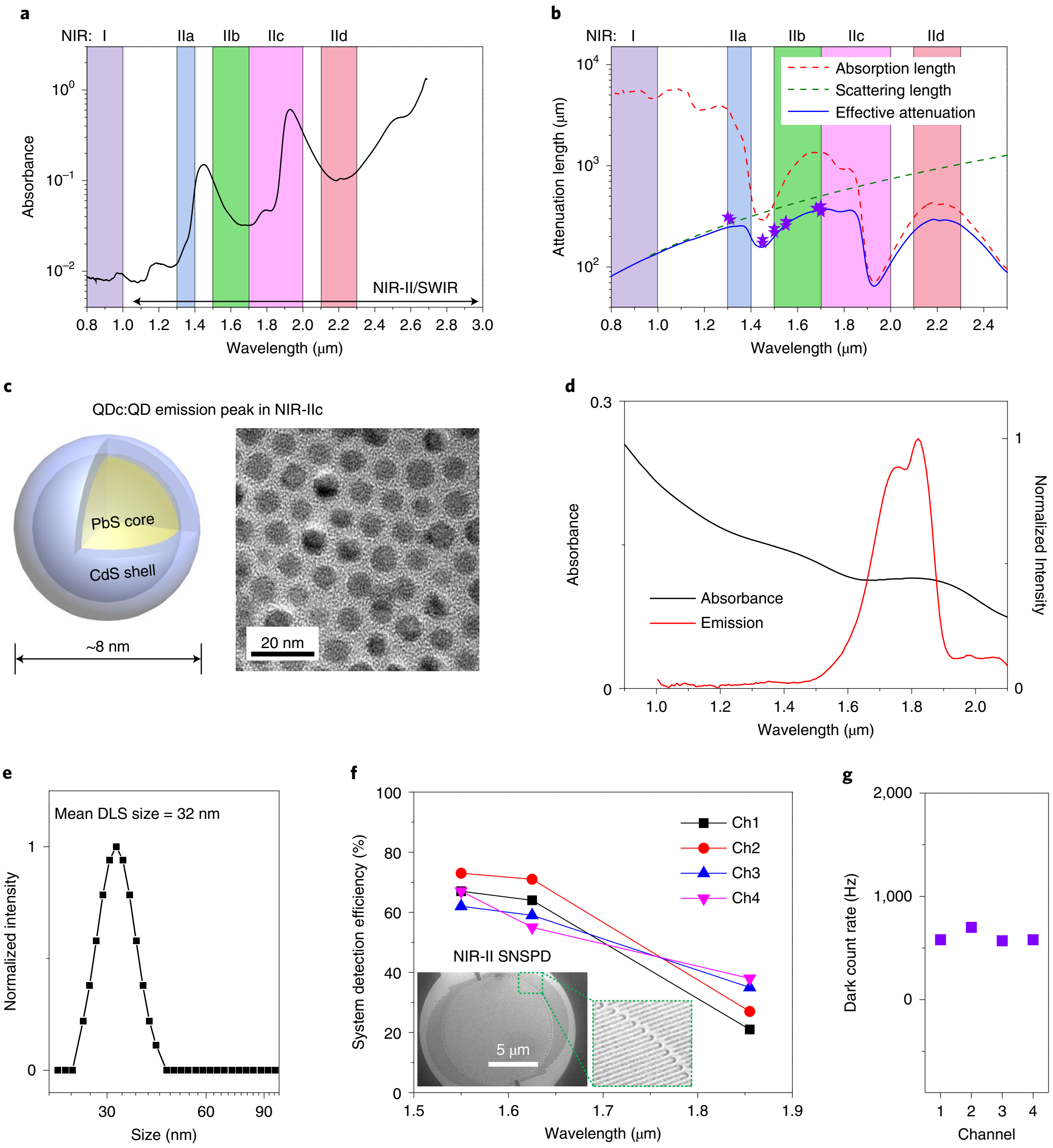

Fig. 1 | Lead sulfide QDs and superconducting nanowire single-photon detectors enabling fluorescence imaging beyond 1,700 nm. a, The absorbance of water measured in a cuvette with 0.1 mm light path by a spectrophotometer. **b**, Wavelength-dependent attenuation length ($1/(1/l_s+1/l_a)$) of brain tissue, where the l_s of the mouse brain was mimicked by 5% intralipid solution ($l_s=0.008\lambda^{-2.4}$)[18]. $l_a=1/\mu_a=L/(D\times\ln 10)$ is the attenuation length of light due to water absorption[39], where μ_a is the absorption coefficient, L is the optical path length and D is absorbance as shown in **a**. The stars represent previously reported effective attenuation lengths of mouse brains measured in vivo[1,40]. **c**, Schematic design of NIR-IIc core–shell PbS/CdS QDs (left) and corresponding transmission electron microscopy image (right). The results are similar for $n=3$ individuals (three batches of newly prepared QDc). **d**, The absorption spectrum of the QDc and emission spectrum of P^3-QDc were measured in tetrachloroethylene and PBS buffer, respectively. A 1 mm cuvette was used. The absorption spectrum was measured in an organic phase as the absorption peak of water at ~1,445 nm influenced the measurement of absorbance in water. **e**, Dynamic light scattering spectra of P^3-QDc in PBS buffer. **f**, Optimized multichannel SNSPD with high system detection efficiency in NIR-IIb (Ch1 and Ch2) and NIR-IIc (Ch3 and Ch4) windows. Insets: a scanning electron microscopy image of a typical SNSPD. **g**, The dark counts of the four SNSPDs used in our experiments.

water absorption becomes overwhelming and through-tissue fluorescence imaging is impossible (Fig. 1a). So far there has been no report of fluorescence imaging by one-photon excitation of living systems at wavelengths >1,700 nm, limited by the lack of biocompatible fluorescent/luminescent probes with sufficient quantum yield/brightness, and that InGaAs cameras/detectors are insensitive to light with wavelengths greater than >1,700 nm in the NIR-IIc/NIR-IId range.

Here we developed aqueous soluble core–shell lead sulfide/cadmium sulfide (PbS/CdS) QDs with emission peaks at ~1,880 nm and employed superconducting nanowire single-photon detectors (SNSPDs) for in vivo imaging at wavelengths >1,700 nm to further suppress light scattering and push the limit of single photons excited through-tissue imaging. Confocal microscopy through mouse tissues in the NIR-IIc window revealed mouse scalp/skull/brain structures in three-dimensions and enabled non-invasive, surgery-free molecular imaging of the peripheral node address (PNAd) on high endothelial venules (HEVs), as well as CD169 + macrophages and CD3 + T cells inside of mouse inguinal lymph nodes (iLNs).

QDs and SNSPDs for NIR-IIc imaging

We synthesized PbS QDs with an emission peak at ~2,009 nm via a modified organometallic route[26]. A CdS shell on the PbS core was then grown via the cation-exchange approach to protect the PbS core from degradation[12]. The shell growth step shifted the emission peak of the core to ~1,880 nm (Supplementary Fig. 2a; see the Methods for the synthesis procedure). The resulting PbS/CdS QDs with an emission peak in NIR-IIc (named QDc herein) showed a narrow size distribution of ~8 nm (Fig. 1c and Supplementary Fig. 2b), which is larger than our previously synthesized ~6.9 nm QDs with an emission peak in NIR-IIb (named QDb)[12]. To transfer the QDc from the organic to the aqueous phase, a hydrophilic polymeric cross-linked network (P^3 coating) developed by our group was coated onto the QDc to impart biocompatibility in physiological environments as well as biliary excretion in about two weeks without apparent toxic effects[14,27]. The final aqueous-stabilized P^3-QDc exhibited a peak emission wavelength of ~1,820 nm in NIR-IIc (Fig. 1d). Dynamic light scattering analysis of the P^3-QDc showed an average hydrodynamic size of ~32 nm in aqueous solutions (Fig. 1e).

The upper spectral detection limit of 1,700 nm for InGaAs detectors was overcome by an SNSPD designed for wavelengths from 1,550 nm to 2,000 nm (Fig. 1f,g). The single-photon detectors were fabricated on an optimized niobium titanium nitride (NbTiN) superconducting film[28] with an optimized superconducting nanowire width and detector geometry (see Supplementary Note 1 for details on the SNSPD). The SNSPDs were connected to our home-built confocal microscope through single-mode fibres transmitting in the 1,200–2,000 nm range (see Methods and Supplementary Figs. 3 and 4), which permitted diffraction-limited resolution in non-scattering media (see the 'resolution analysis' section in the Methods).

Phantom imaging in NIR-IIb and NIR-IIc sub-windows

We first imaged a 50-µm-diameter capillary filled with aqueous suspensions of P^3-QDb or P^3-QDc—with emission peaks residing in the NIR-IIb (1,500–1,700 nm)[12] or NIR-IIc (1,700–2,000 nm) regions—immersed in a ~5% intralipid solution that mimicked blood vessels in a mouse brain tissue (Fig. 2a–c). NIR-IIc fluorescence was collected at 1,800–2,000 nm (see Methods for the filters used), but at millimetre imaging depths the actual upper limit was ~1,900 nm, set by water absorption (Fig. 1a). This upper limit was also obtained on the basis that the detected fluorescence signals of QDc through 2–10-mm-thick layers of water showed diminished >1,900 nm signals due to water absorption (Fig. 2d), whereas emission was clearly detected in the 1,600–1,850 nm range, even through a 10-mm-thick water layer. We set the upper limit of NIR-IIc to 2,000 nm, as the 1,850–2,000 nm emission could still be detected for imaging shallower layer of tissues in vivo. For wide-field imaging of QDb-filled capillaries in the NIR-IIb range with an InGaAs camera (excitation = 808 nm), the capillary was resolved at up to a ~3.2 mm immersion depth in the intralipid solution with an SBR of 1.28, but the SBR was low (~1) at 4.4 mm depth (Fig. 2a, first column; Supplementary Fig. 5). Confocal microscopy imaging (with a 10× objective and z resolution ≈ 18 µm) in the same 1,500–1,700 nm range using the SNSPD (at 1,319 nm laser excitation) afforded improved SBRs over InGaAs camera imaging at imaging depths <2.3 mm (Fig. 2c), but was incapable of resolving the capillary at depths beyond ~2.6 mm (Fig. 2a, second column). The side lobes around the capillary in the wide-field images were attributed to scattered light and can be rejected by confocal microscopy (Fig. 2a), but with a sacrifice of temporal resolution due to raster scanning being required. Wide-field imaging is advantageous in simplicity and fast imaging. Confocal microscopy (1,800–2,000 nm emission; 1,540 nm excitation) imaging of QDc-filled capillaries in NIR-IIc using the SNSPD extended the imaging depth to ~3.2 mm (Fig. 2a, third column). When a 1,650 nm laser was used for NIR-IIc excitation, the highest SBR was achieved at all depths (Fig. 2c) and the capillary was resolved at up to ~4.4 mm (Fig. 2a, fourth column), deeper than NIR-IIc imaging at 1,540 nm excitation and NIR-IIb imaging at 1,319 nm excitation.

Monte Carlo simulations[29] revealed light spreading laterally (along x) and intensity decaying longitudinally (along z) due to tissue absorption and scattering through a tissue-mimicking medium (Supplementary Fig. 6a); the spreading effect reduced for longer-wavelength light (Supplementary Fig. 6b). The 1,540 nm laser experienced less scattering but decayed faster than the 1,319 nm laser due to ~4.4-times-higher absorption (Fig. 1a). Due to the combined absorption and scattering effects, the 1,650 nm laser transmitting through a turbid medium exhibited the lowest decay in intensity and the lowest beam broadening compared with the other wavelength lasers (800 nm, 1,000 nm, 1,319 nm and 1,540 nm; Supplementary Fig. 6), which was ideal for NIR-IIc imaging to optimize the penetration depths of both the excitation and emission light through biological tissues.

Intact mouse head imaging in NIR-IIb and NIR-IIc sub-windows

Following tail-vein injection of P^3-QDc, we performed NIR-IIc non-invasive three-dimensional confocal imaging of blood vessels through intact mouse heads (Fig. 3a,b). The circulating P^3-QDc-labelled blood vessels in intact mouse head layers (including the scalp, skull, meninges and a ~550-µm- or ~900-µm-thick brain cortex) were resolved by three-dimensional volumetric NIR-IIc imaging at depths of up to ~800 µm or 1,100 µm at 1,540 nm or 1,650 nm laser excitations, respectively (Fig. 3b; see Supplementary Video 1 for three-dimensional views). Vessel-like channels through the meninges connecting the skull and brain cortex were observed (Fig. 3b, indicated by arrows). These vessels/channels were shown to be important for the brain's immune response to injuries and infections[30].

Note that both NIR-IIc confocal microscopy and NIR-IIb LSM[18] can reject scattered and out-of-focus light, enabling high-contrast three-dimensional imaging of mouse heads. NIR-II LSM allowed faster imaging speeds using wide-field detection, but the spectral detection wavelength was <1,700 nm with InGaAs cameras, limiting the imaging depth for resolving small features in mouse brains. Through an intact mouse head, the NIR-IIb LSM at 1,319 nm excitation reached ~250 µm depth in the cortex[18], whereas NIR-IIc confocal imaging at 1,650 nm excitation reached ~900 µm depth in the cortex.

We compared an SNSPD with a commercial 900–1,700 nm photomultiplier tube (PMT) for non-invasive confocal microscopy imaging through an intact mouse head. A mouse was intravenously injected with P^3-QDb and P^3-QDc, sequentially, 30 min before imaging, and excited by 1,319 nm, 1,540 nm and 1,650 nm lasers at the same power (28.5 mW at the head surface; see Supplementary Note 2 for a power analysis and Supplementary Table 1 for detailed experimental conditions). For NIR-IIb imaging at a laser excitation of 1,319 nm, the SNSPD-based confocal microscopy resolved small capillary vessels that were not detected by PMT and allowed higher spatial resolutions at greater imaging depths (Fig. 3c, first versus second column; Fig. 3d). At a laser excitation of 1,540 nm, imaging in the NIR-IIc window afforded better resolution than in the NIR-IIb region at 1,319 nm using the same SNSPD (Fig. 3c,

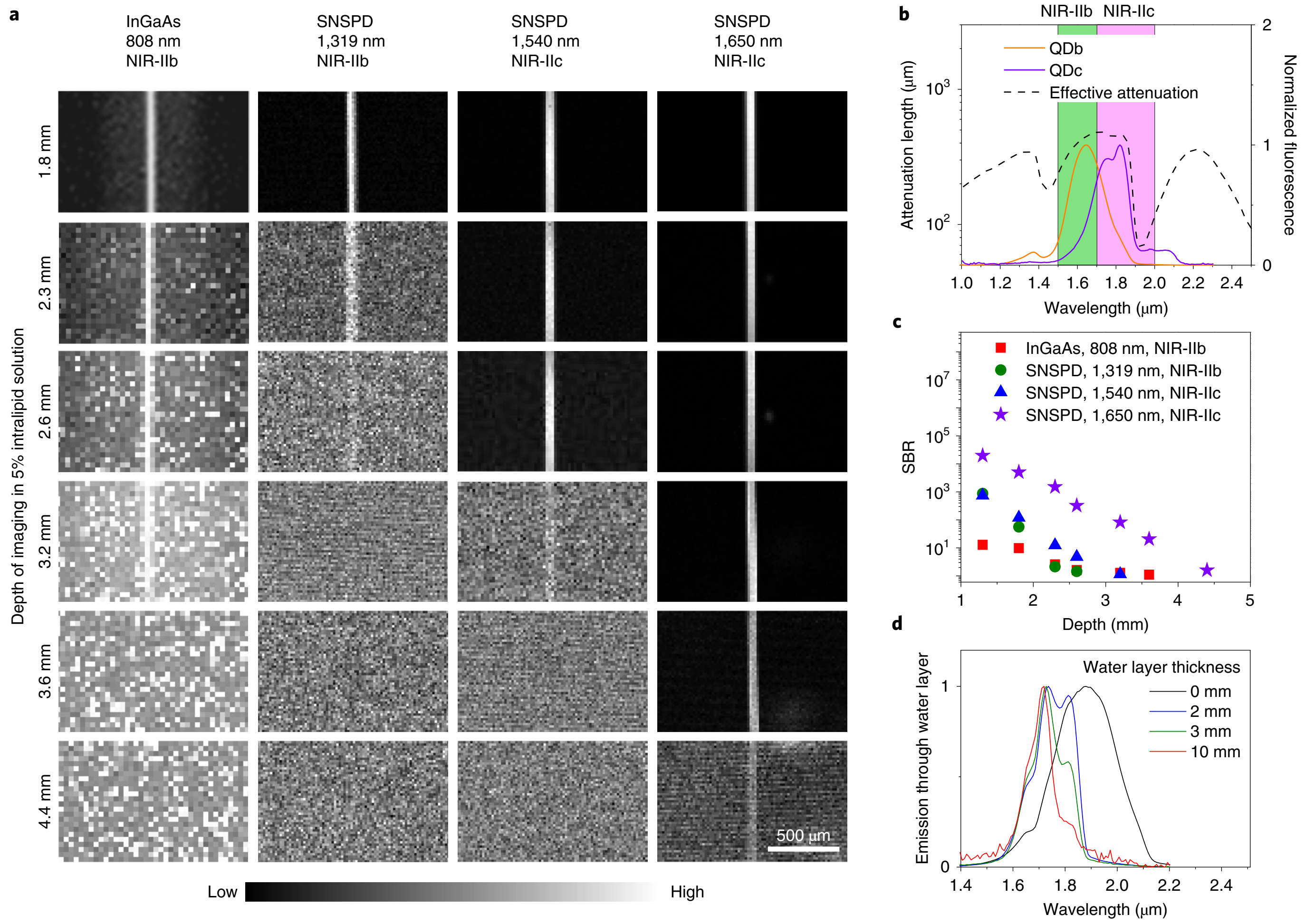

Fig. 2 | Fluorescence imaging in NIR-IIb and NIR-IIc windows. a, Fluorescence imaging of a 50-μm-diameter capillary tube—filled with NIR-IIb QDb or NIR-IIc QDc, immersed at different depths in 5% intralipid solution—by a wide-field system with a two-dimensional InGaAs camera, or a confocal microscope with SNSPDs. The 50-μm-diameter capillary tubes immersed in 5% intralipid solution mimicked blood vessels in mouse brain tissues. An 808 nm laser was used for NIR-IIb wide-field imaging. A 1,319 nm laser was applied for NIR-IIb confocal microscopy. A 1,540 nm laser or a 1,650 nm laser and a 10× objective (NA = 0.25) were used for NIR-IIc confocal microscopy. NIR-IIb and NIR-IIc fluorescence was collected at 1,500–1,700 nm and 1,800–2,000 nm, respectively. These three lasers had the same power (28.5 mW) at the intralipid surface. The results were similar for $n = 3$ individual experiments. **b**, Fluorescence spectra of P^3-QDb and P^3-QDc in PBS, with emission peaks in the NIR-IIb[12] and NIR-IIc regions, respectively. A cuvette with 1 mm light path was used to measure the spectra. The effective attenuation length is from Fig. 1b. **c**, Comparison of SBR of the results shown in **a**. The SBR of the wide-field results was from the ratio of the capillary brightness to the signal from the side lobe around the capillary. **d**, Emission spectra of NIR-IIc QDc in a cuvette measured under water at depths of 2 mm, 3 mm and 10 mm. The 0 mm data indicate no water layer, and the emission spectrum was measured with QDc in tetrachloroethylene without any influence from water.

second versus third column; Fig. 3d). We then compared the 1,650 nm and 1,540 nm lasers for NIR-IIc imaging using the same SNSPD; 1,650 nm excitation showed an apparent improvement on resolution quantified by the full-width at half-maximum (FWHM) of features, SBR and penetration depth (Fig. 3c, third versus fourth column; Fig. 3d,e). The wider broadening of the point spread function (PSF) at shorter wavelengths was evaluated by the blurred edges of blood vessels[8]. The FWHM of a vessel imaged at $z = 400\,\mu$m was measured to be 6.2 μm, 5.3 μm and 3.4 μm by SNSPD-based confocal microscopy using 1,319 nm, 1,540 nm and 1,650 nm lasers, respectively, for NIR-IIb or NIR-IIc imaging (Fig. 3d, left), suggesting increased spatial resolution. As the imaging depth increased to 700 μm, vessels not resolved by PMT were resolved by SNSPD in NIR-IIb and NIR-IIc windows (Fig. 3c). Only the 1,650-nm-laser-excited NIR-IIc imaging allowed imaging into the mouse head at depths beyond 1,100 μm. Confocal microscopy in the NIR-IIc window at 1,650 nm excitation with SNSPD afforded the highest contrast, with a SBR of ~170 at $z = 400\,\mu$m, which decreased to ~5 at 1,100 μm—approximately 3.3-, 3.3- and 11.5-times higher than NIR-IIc imaging at 1,540 nm excitation with SNSPD, NIR-IIb imaging at 1,319 nm with SNSPD, and NIR-IIb imaging at 1,319 nm with PMT, respectively (Fig. 3e).

To assess the fastest scan rate possible by our current NIR-IIc confocal microscopy with 1,650 nm excitation with various powers, we performed blood vessel imaging in mouse brain ex vivo. A scan rate of ~3 Hz (pixels = 133 × 200; scan area = 185 μm × 278 μm) was achieved down to 0.67 mW (Supplementary Fig. 7), and limited by the galvo mirror scan rate (~600 Hz at this scan area and pixels) and probe brightness.

Non-invasive in vivo NIR-IIc confocal microscopy of mouse iLNs

The lymphatic system plays crucial roles in immune responses to infections, cancer and vaccination. It is highly desirable to image

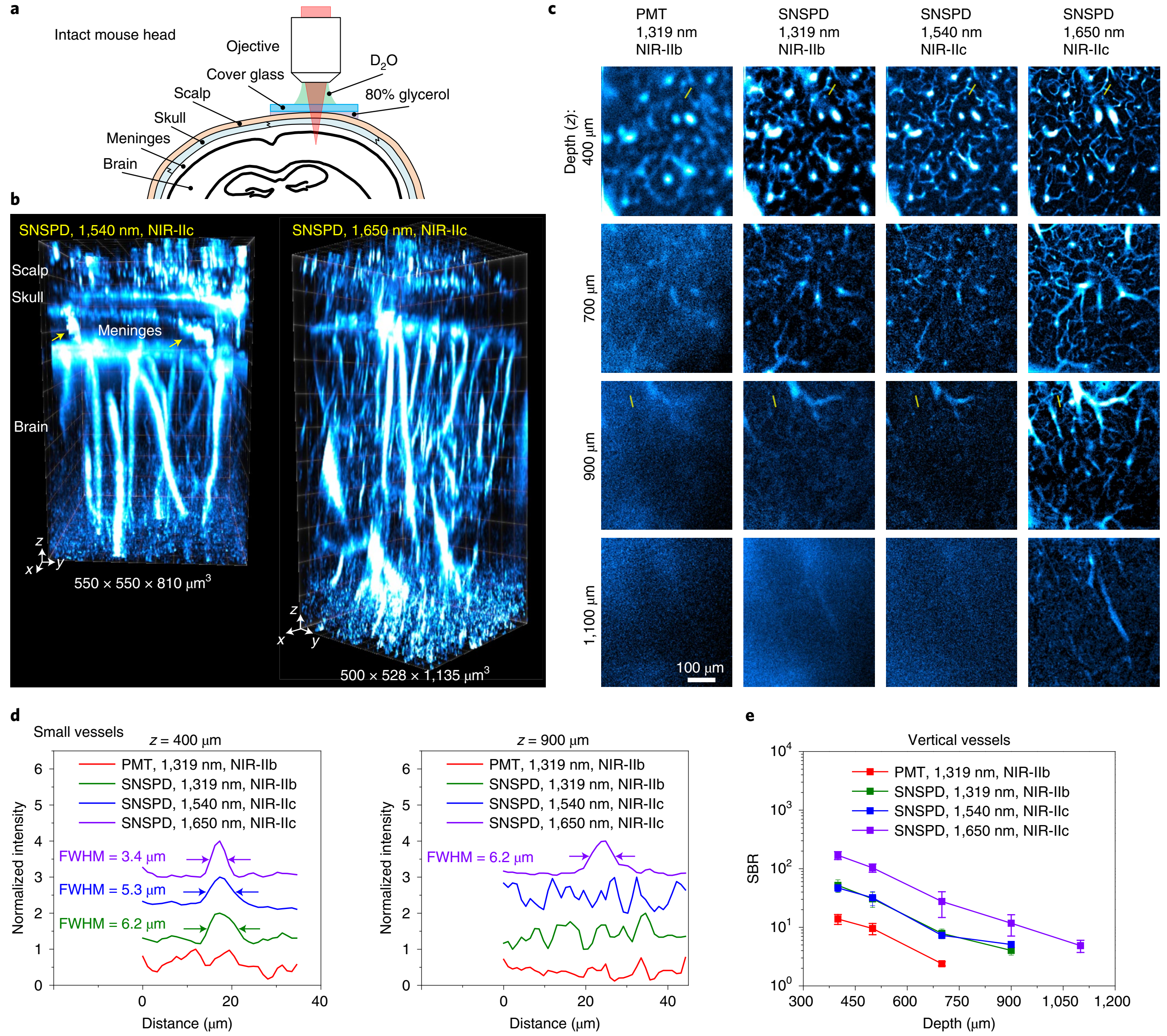

Fig. 3 | Non-invasive in vivo confocal microscopy of intact mouse head in NIR-IIc window. a, Schematic of intact mouse head imaging in NIR-IIc window. The gap between the ~170-μm-thick cover glass and the mouse head was filled with 80% glycerol. We used a 25× objective (NA = 1.05) and D_2O as the immersion liquid. **b**, Three-dimensional volumetric images of blood vessels in an intact mouse head visualized through the scalp, skull, meninges and brain cortex, obtained with a 5 μm *z*-scan increment. The arrows indicate vessel-like channels connecting the skull and brain cortex in the meninges. Confocal microscopy was performed 30 min after intravenous injection of P^3-QDc. Left: fluorescence signal was collected in 1,750–2,000 nm window and excited by a 1,540 nm laser. Right: a 1,650 nm laser was used and fluorescence was collected in 1,800–2,000 nm window. **c**, High-resolution confocal images of blood vessels at various depths through intact mouse head imaged with a PMT or SNSPD in NIR-IIb or NIR-IIc window. Imaging was performed 30 min after intravenous injection of P^3-QDb and P^3-QDc, sequentially. NIR-IIb and NIR-IIc fluorescence was collected at 1,500–1,700 nm and 1,800–2,000 nm windows and excited by 1,319 nm, 1,540 nm and 1,650 nm lasers. These three lasers had the same power (28.5 mW) at the mouse head surface. **b**,**c**, The results were similar for *n* = 3 individuals (BALB/c, female, three weeks old). **d**, Normalized photon counts profiles along the yellow lines in **c**. **e**, Comparison of SBR for *xy* images recorded at different depths by confocal microscopy with a PMT or SNSPD in different windows. The signals of vertical vessels were used to calculate the SBR as these vessels existed from the surface of brain cortex to the deepest layer of imaging. Data are shown as mean ± s.d. derived from analysing ≥4 vessels at each depth.

and monitor cellular immunological events within the lymph nodes in real-time and over-time longitudinally at cellular resolution. Here we imaged lymph nodes though intact mouse skin, which differed from previous intravital microscopy with installed transparent windows by invasive surgery[4,31,32].

We first performed non-invasive in vivo NIR-IIc molecular imaging of the PNAd on HEVs in mouse iLNs (Fig. 4a–e). We conjugated anti-MECA-79 antibodies to P^3-QDc (aMECA-79-QDc), intravenously injected into a mouse through the tail-vein, and 24 h later injected an organic probe (p-FE; excitation = 808 nm;

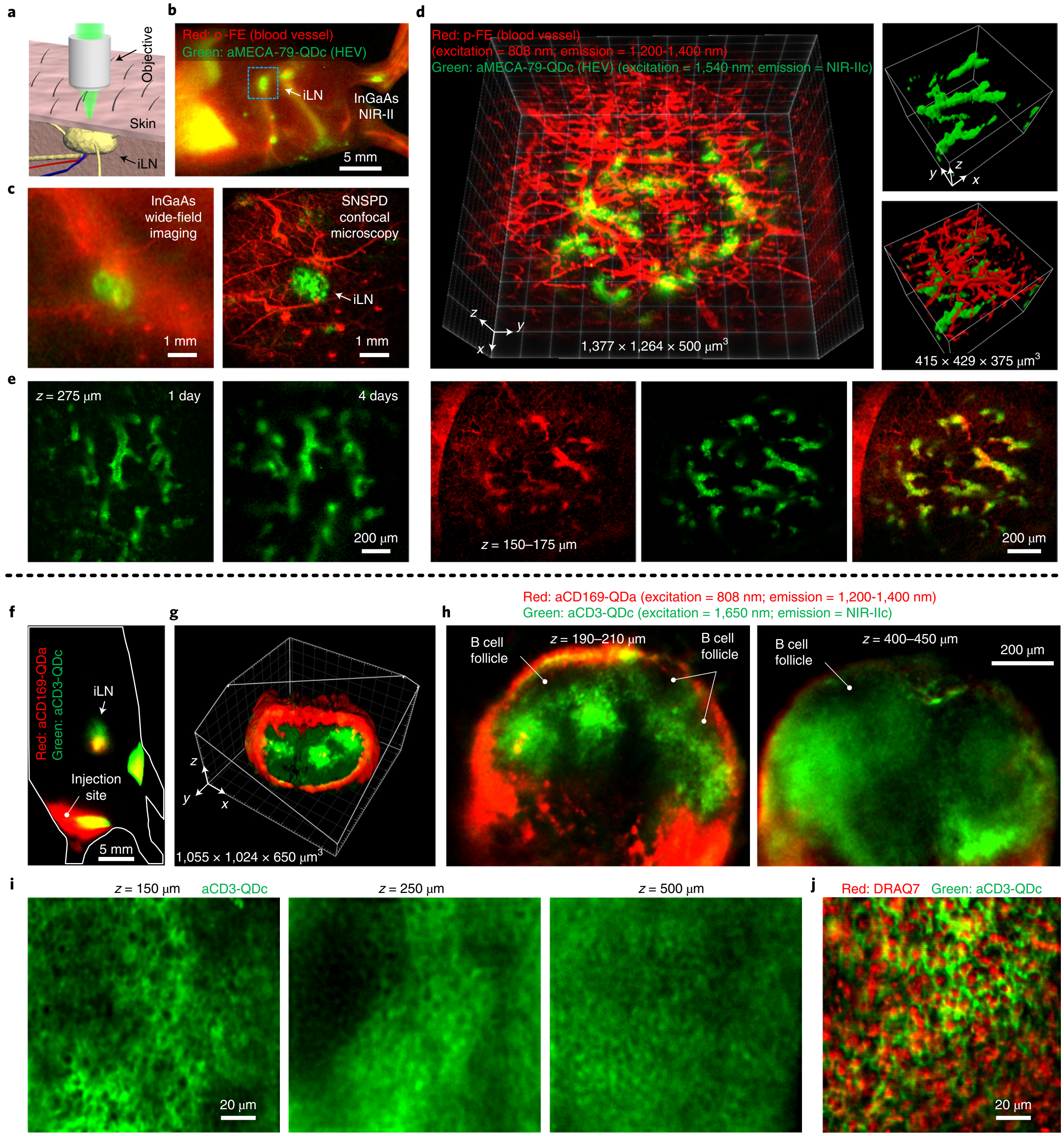

Fig. 4 | Non-invasive in vivo NIR-II confocal microscopy of mouse iLNs. a, Schematic of non-invasive imaging of iLNs by confocal microscopy. **b**, Wide-field imaging of p-FE-labelled blood vessels and aMECA-79-QDc-labelled HEVs one day after intravenous injection of aMECA-79-QDc and 10 min after intravenous injection of free p-FE. **c**, Comparison of wide-field imaging and confocal microscopy of the iLN marked by the rectangle in **b** at a higher magnification. An 808 nm laser was used for wide-field imaging to excite p-FE and aMECA-79-QDc. For confocal microscopy, p-FE and aMECA-79-QDc were excited by 808 nm and 1,540 nm lasers, respectively. **d**, Confocal microscopy of blood vessels and HEVs labelled by aMECA-79-QDc in iLNs. Skin layer vessels (red) and underlying HEVs (green) in iLNs were resolved. **e**, Longitudinal observation of aMECA-79-QDc-labelled HEVs in iLNs one and four days after intravenous injection. To image the same iLN multiple times, we first located the iLN by wide-field imaging of aMECA-79-QDc. We then focused on the iLN for confocal microscopy as only the iLN showed a strong fluorescence signal owing to the antibody-QDc-labelled HEVs. **f**, Wide-field imaging of aCD169-QDa and aCD3-QDc one day after subcutaneous injection at the base of tail. **g**, Three-dimensional volumetric imaging of CD169 + macrophages (aCD169-QDa) and CD3 + T cells (aCD3-QDc) in iLNs by confocal microscopy of the iLN shown in **f**. **h**, Maximum-intensity *z*-projections for a 20-μm- or 50 μm-thick volume along *z* at $z = 200$ μm and 425 μm, respectively. **i**, High-resolution confocal microscopy of CD3 + T cells in iLNs 24 h after subcutaneous injection of aCD3-QDc. **j**, Ex vivo confocal microscopy imaging of nucleus and CD3 + T cells (aCD3-QDc) in iLNs. The results were similar for $n = 3$ (**b**,**c**,**f**–**j**) and $n = 11$ (**d**) individuals (BALB/c, female, three weeks old). See Supplementary Table 1 for detailed experimental conditions.

emission = 1,200–1,400 nm)[20] as a blood vessel NIR-II imaging agent. The MECA-79 antibody was known to specifically target the 6-sulfo sialyl Lewis X epitope on PNAds expressed on HEVs[33]. We first performed wide-field imaging in NIR-IIb (the QDc exhibited emission in both NIR-IIb and NIR-IIc) ten minutes after injection of p-FE and observed anti-MECA-79-targeted QDc emission in the iLNs, with blood vessels labelled by circulating p-FE imaged in the 1,200–1,400 nm emission range (Fig. 4b; Fig. 4c, left). By comparison, no QDc emission signal was detected in the iLNs in control mice injected with free P^3-QDc without anti-MECA-79 conjugation (Supplementary Fig. 8a). Free P^3-QDc cleared from the liver faster than the aMECA-79-QDc (Supplementary Fig. 8a–c). This could be as normal livers are known to overexpress MECA-79 sulfated glycans[34], leading to stronger signals and longer retention of aMECA-79-QDc. To further confirm specific targeting of aMECA-79-QDc to HEVs, we injected free MECA-79 antibodies 24 h before aMECA-79-QDc injection as a blocking experiment. In another control, we injected TRC105-QDc intravenously (TRC105 is an irrelevant antibody to PNAd; it targets endoglin overexpressed on proliferating endothelial cells[35]). In both cases we did not observe an apparent NIR-IIc signal in the iLNs (Supplementary Fig. 8d,e), confirming specific molecular targeting of HEVs in lymph nodes with aMECA-79-QDc injected intravenously.

Next we mapped out/differentiated the spatial distributions of blood vessels (with circulating p-FE dye) and HEVs (aMECA-79-QDc) in the iLNs. At low magnifications the iLN region was imaged by an InGaAs wide-field system and SNSPD confocal microscopy (Fig. 4c). The latter clearly rejected scattering-induced backgrounds and allowed weak signal detection in both the 1,200–1,400 nm and NIR-IIc windows. High-resolution three-dimensional confocal imaging revealed HEVs in the iLNs below the skin layer, with p-FE labelling the skin blood vessels (Fig. 4d; Supplementary Figs. 9 and 10). Confocal imaging at different depths in vivo and ex vivo showed that only HEVs were labelled by aMECA-79-QDc, whereas both HEVs and the surrounding blood vessels in the iLNs were labelled by p-FE (Fig. 4d; Supplementary Figs. 9 and 10), confirming specific targeting of HEVs by aMECA-79-QDc. Confocal microscopy in NIR-IIc with 1,540 nm excitation (Supplementary Fig. 9) or 1,650 nm excitation (Supplementary Figs. 10) allowed iLN molecular imaging with a penetration depth of ~500 µm, including the skin layer, which is around two-times deeper than in the 1,200–1,400 nm range. The penetration depths for 1,540 nm or 1,650 nm excitations were similar, ~500 µm, on the order of the size of the iLN in z-direction. Comparatively a lower power was needed for the 1,650 nm excitation to reach such depth (1.6–10.0 mW versus 35 mW). The stabilities of P^3-QDc and aMECA-79-QDc afforded lasting targeting effects, allowing for non-invasive NIR-IIc confocal microscopy imaging of HEVs in iLNs, longitudinally, over more than four days (Fig. 4e).

To achieve non-invasive in vivo NIR-IIc confocal microscopy imaging at cellular resolutions, we performed two-colour molecular imaging of CD169 (expressed on subcapsular-sinus macrophages) and CD3 (on T cells) in intact mouse iLNs. We conjugated CD169 antibodies to QDs with peak emissions at 1,110 nm (aCD169-QDa), and CD3 antibodies to P^3-QDc (aCD3-QDc), and subcutaneously injected them at the base of the tail, sequentially. One day after injection, wide-field images showed strong aCD169-QDa and aCD3-QDc signals in iLNs (Fig. 4f). Two-colour large-area confocal microscopy (Fig. 4g,h) revealed CD169 + macrophages labelled by aCD169-QDa outlining the subcapsular sinus; with CD3 + T cells in the T cell zone in the interior of the lymph node labelled by aCD3-QDc. Unlabelled B cell follicles were also recognizable (dark regions in Fig. 4h) as they were close to the layer of macrophages and surrounded by T cells[36,37]. High-resolution confocal microscopy imaging of CD3 + T cells in the NIR-IIc window at 1,650 nm excitation resolved T cells labelled on the outside of the cells (dark in the middle) as deep as 500 µm in the intact iLNs (Fig. 4i). Ex vivo, we stained cell nuclei with DRAQ7 dye (see Methods). Ex vivo confocal microscopy of DRAQ7 and aCD3-QDc (Fig. 4j) clearly resolved T cells outlined by aCD3-QDc with DRAQ7 labels inside the nuclei. These results established non-invasive NIR-IIc confocal microscopy imaging at cellular resolution in intact lymph nodes in vivo.

Conclusion

NIR-IIc confocal microscopy with single-photon detectors afforded non-invasive cellular-resolution imaging through intact mouse heads and lymph nodes longitudinally. Our one-photon excitation NIR-IIc confocal microscopy employed 1,650 nm excitation, close to the longest excitation wavelength of ~1,700 nm used for two-photon or three-photon microscopy[1,7]. These similar excitation lights undergo similar decays when transmitting through the thickness z of a tissue. However, although fluorescence emission in one-photon excitation microscopy scales linearly with light intensity $I(z)$, two-photon and three-photon fluorescence are nonlinear, scaling with the second and third power of the excitation light, respectively, and decay more rapidly than the one-photon case[38]. NIR-IIc confocal microscopy provides an alternative method to multiphoton microscopy at a lower cost (Supplementary Table 2). Integrating NIR-IIc confocal microscopy and multiphoton microscopy with ~1,650–1,700 nm excitation could allow multichannel imaging of complex biological systems using a broader range of probes. In terms of laser safety, we note that all of the approximately 60 mice used for in vivo imaging through this work were safe and healthy post imaging, without signs of laser-induced skin burns (redness, scars and so on). None of the mice showed any abnormal behaviour, or signs of pain or discomfort after imaging. None of the mice had to be sacrificed after imaging. Furthermore, we employed an approach of linearly increasing the laser power at increasing tissue depths to stay below the 1 J cm^{-2} laser safety limit of a 1,650 nm laser (American National Standard for Safe Use of Lasers, ANSI Z136.1) while maximizing the imaging signal (Supplementary Note 2). It is also important to note that the laser power/fluence needed for imaging depends on the brightness of the dyes/probes used. Although our current QDc are sufficiently bright for in vivo imaging within the safety limit, new advances in probe development could allow safe imaging much below the 1 J cm^{-2} limit.

Online content

Any methods, additional references, Nature Research reporting summaries, source data, extended data, supplementary information, acknowledgements, peer review information; details of author contributions and competing interests; and statements of data and code availability are available at https://doi.org/10.1038/s41565-022-01130-3.

Received: 13 October 2021; Accepted: 31 March 2022;
Published online: 23 May 2022

References

1. Horton, N. G. et al. In vivo three-photon microscopy of subcortical structures within an intact mouse brain. *Nat. Photon.* **7**, 205–209 (2013).
2. Yildirim, M., Sugihara, H., So, P. T. C. & Sur, M. Functional imaging of visual cortical layers and subplate in awake mice with optimized three-photon microscopy. *Nat. Commun.* **10**, 177 (2019).
3. Kobat, D., Horton, N. & Xu, C. In vivo two-photon microscopy to 1.6-mm depth in mouse cortex. *J. Biomed. Opt.* **16**, 106014 (2011).
4. Miller, M. J., Wei, S. H., Parker, I. & Cahalan, M. D. Two-photon imaging of lymphocyte motility and antigen response in intact lymph node. *Science* **296**, 1869–1873 (2002).
5. Helmchen, F. & Denk, W. Deep tissue two-photon microscopy. *Nat. Methods* **2**, 932–940 (2005).
6. Svoboda, K. & Yasuda, R. Principles of two-photon excitation microscopy and its applications to neuroscience. *Neuron* **50**, 823–839 (2006).

7. Horton, N. G. & Xu, C. Dispersion compensation in three-photon fluorescence microscopy at 1,700 nm. *Biomed. Opt. Exp.* **6**, 1392–1397 (2015).
8. Wang, T. et al. Three-photon imaging of mouse brain structure and function through the intact skull. *Nat. Methods* **15**, 789–792 (2018).
9. Yang, Q. et al. Donor engineering for NIR-II molecular fluorophores with enhanced fluorescent performance. *J. Am. Chem. Soc.* **140**, 1715–1724 (2018).
10. Li, Y. et al. Design of AIEgens for near-infrared IIb imaging through structural modulation at molecular and morphological levels. *Nat. Commun.* **11**, 1255 (2020).
11. Welsher, K. et al. A route to brightly fluorescent carbon nanotubes for near-infrared imaging in mice. *Nat. Nanotechnol.* **4**, 773–780 (2009).
12. Zhang, M. et al. Bright quantum dots emitting at ~1,600 nm in the NIR-IIb window for deep tissue fluorescence imaging. *Proc. Natl Acad. Sci. USA* **115**, 6590–6595 (2018).
13. Bruns, O. T. et al. Next-generation in vivo optical imaging with short-wave infrared quantum dots. *Nat. Biomed. Eng.* **1**, 0056 (2017).
14. Zhong, Y. et al. In vivo molecular imaging for immunotherapy using ultra-bright near-infrared-IIb rare-earth nanoparticles. *Nat. Biotechnol.* **37**, 1322–1331 (2019).
15. Fan, Y. et al. Lifetime-engineered NIR-II nanoparticles unlock multiplexed in vivo imaging. *Nat. Nanotechnol.* **13**, 941–946 (2018).
16. Naczynski, D. J. et al. Rare-earth-doped biological composites as in vivo shortwave infrared reporters. *Nat. Commun.* **4**, 2199 (2013).
17. Zhu, S. et al. 3D NIR-II molecular imaging distinguishes targeted organs with high-performance NIR-II bioconjugates. *Adv. Mater.* **30**, 1705799 (2018).
18. Wang, F. et al. Light-sheet microscopy in the near-infrared II window. *Nat. Methods* **16**, 545–552 (2019).
19. Wang, F. et al. In vivo NIR-II structured-illumination light-sheet microscopy. *Proc. Natl Acad. Sci. USA* **118**, e2023888118 (2021).
20. Wan, H. et al. A bright organic NIR-II nanofluorophore for three-dimensional imaging into biological tissues. *Nat. Commun.* **9**, 1–9 (2018).
21. Golovynskyi, S. et al. Optical windows for head tissues in near-infrared and short-wave infrared regions: approaching transcranial light applications. *J. Biophoton.* **11**, e201800141 (2018).
22. Hong, G. et al. Through-skull fluorescence imaging of the brain in a new near-infrared window. *Nat. Photon.* **8**, 723–730 (2014).
23. Burrows, P. E. et al. Lymphatic abnormalities are associated with RASA1 gene mutations in mouse and man. *Proc. Natl Acad. Sci. USA* **110**, 8621–8626 (2013).
24. Diao, S. et al. Fluorescence imaging in vivo at wavelengths beyond 1,500 nm. *Angew. Chem. Int. Ed.* **54**, 14758–14762 (2015).
25. Pasko, J., Shin, S. & Cheung, D. *Epitaxial HgCdTe/CdTe Photodiodes For The 1 to 3 pm Spectral Region* 0282 TSE (SPIE, 1981).
26. Ren, F., Zhao, H., Vetrone, F. & Ma, D. Microwave-assisted cation exchange toward synthesis of near-infrared emitting PbS/CdS core/shell quantum dots with significantly improved quantum yields through a uniform growth path. *Nanoscale* **5**, 7800–7804 (2013).
27. Ma, Z. et al. Cross-link-functionalized nanoparticles for rapid excretion in nanotheranostic applications. *Angew. Chem.* **132**, 20733–20741 (2020).
28. Zichi, J. et al. Optimizing the stoichiometry of ultrathin NbTiN films for high-performance superconducting nanowire single-photon detectors. *Opt. Exp.* **27**, 26579–26587 (2019).
29. Wang, L., Jacques, S. L. & Zheng, L. MCML—Monte Carlo modeling of light transport in multi-layered tissues. *Comput. Meth. Prog. Biomed.* **47**, 131–146 (1995).
30. Herisson, F. et al. Direct vascular channels connect skull bone marrow and the brain surface enabling myeloid cell migration. *Nat. Neurosci.* **21**, 1209–1217 (2018).
31. Pereira, E. R. et al. Lymph node metastases can invade local blood vessels, exit the node, and colonize distant organs in mice. *Science* **359**, 1403–1407 (2018).
32. Sewald, X. et al. Retroviruses use CD169-mediated trans-infection of permissive lymphocytes to establish infection. *Science* **350**, 563–567 (2015).
33. Milutinovic, S., Abe, J., Godkin, A., Stein, J. V. & Gallimore, A. The dual role of high endothelial venules in cancer progression versus immunity. *Trends Cancer* **7**, 214–225 (2021).
34. Hoshino, H. et al. Apical membrane expression of distinct sulfated glycans represents a novel marker of cholangiolocellular carcinoma. *Lab. Invest.* **96**, 1246–1255 (2016).
35. Fonsatti, E. & Maio, M. Highlights on endoglin (CD105): from basic findings towards clinical applications in human cancer. *J. Transl. Med.* **2**, 18 (2004).
36. Gaya, M. et al. Inflammation-induced disruption of SCS macrophages impairs B cell responses to secondary infection. *Science* **347**, 667–672 (2015).
37. Girard, J.-P., Moussion, C. & Förster, R. HEVs, lymphatics and homeostatic immune cell trafficking in lymph nodes. *Nat. Rev. Immunol.* **12**, 762–773 (2012).
38. Gu, M., Gan, X., Kisteman, A. & Xu, M. G. Comparison of penetration depth between two-photon excitation and single-photon excitation in imaging through turbid tissue media. *Appl. Phys. Lett.* **77**, 1551–1553 (2000).
39. Hu, C., Muller-Karger, F. E. & Zepp, R. G. Absorbance, absorption coefficient, and apparent quantum yield: a comment on common ambiguity in the use of these optical concepts. *Limnol. Oceanogr.* **47**, 1261–1267 (2002).
40. Wang, M. et al. Comparing the effective attenuation lengths for long wavelength in vivo imaging of the mouse brain. *Biomed. Opt. Exp.* **9**, 3534–3543 (2018).

Methods

Materials. Lead (II) chloride ($PbCl_2$), 1-octadecene, cadmium oxide (CdO) and sulfur powder (sublimed) were purchased from Alfa Aesar. Oleylamine, oleic acid, 1-octadecene, poly(maleic anhydride-alt-1-octadecene) (PMH; average molecular weight = 30–50 kDa), 4-morpholineethanesulfonic acid (MES), 4-(dimethylamino) pyridine, poly(acrylic acid) (PAA; average molecular weight = 1.8 kDa), 1-(3-dimethylaminopropyl)-3-ethylcarbodiimide hydrochloride (EDC) and 2-amino-2-(hydroxymethyl)-1,3-propanediol (tris-base) were purchased from Sigma-Aldrich. Hexane, toluene, chloroform, and deionized water were purchased from Fisher Scientific. Methoxy polyethylene glycol amine (mPEG-NH_2; average molecular weight = 5 kDa) was purchased from Laysan-Bio; 8Arm polyethylene glycol amine (8Arm-PEG-NH_2•HCl; average molecular weight = 40 kDa) was purchased from Advanced Biochemicals. All of the chemicals were used without further purification; 50 µm capillaries were bought from VitroCom. Purified anti-mouse/human PNAd antibodies (clone: MECA-79), purified anti-mouse CD169 antibodies (clone: 3D6.112) and DRAQ7 (no. 424001) were purchased from BioLegend. Anti-mouse CD3 antibodies (Clone: KT3) were bought from Bio X Cell.

Synthesis of NIR-IIc PbS/CdS QDs. The synthesis of NIR-IIb PbS/CdS QDb can be found in ref. [12]. This work developed the synthesis of NIR-IIc PbS/CdS QDc.

The core PbS QDs were synthesized using a modified organometallic method[12,26]. In a typical reaction, sulfur precursor solution was prepared by mixing 0.08 g (5 mmol) of sulfur powder and 7.5 ml of oleylamine in a two-neck flask at 120 °C under argon for 30 min.

Synthesis of PbS QDs. $PbCl_2$ (1.668 g, 3 mmol) and oleylamine (15 ml) were mixed in a three-neck flask and degassed for 30 min at 120 °C. The solution was then heated to 165 °C under argon and kept at that temperature for 15 min; 4.5 ml of the sulfur precursor solution (1.5 mmol of sulfur) was injected into the lead precursor solution (6 mmol of lead) under stirring. The temperature was maintained at 165 °C throughout the reaction.

After 180 min, the reaction was quenched by adding 20 ml of cold hexane and 30 ml ethanol. The products were collected by centrifugation and resuspended in a mixture of 15 ml hexane and 30 ml oleic acid. The QDs were precipitated via centrifugation after agitated for 10 min. This precipitation procedure with hexane and oleic acid was repeated three times. The QDs were resuspended in 20 ml toluene after centrifugation.

Synthesis CdS shell on PbS QDs. CdO (1.2 g, 9.2 mmol), oleic acid (8 ml) and 1-octadecene (20 ml) were mixed in a three-neck flask and heated to 200 °C for 1.5 h under argon. The solution was then cooled down to 100 °C and degassed under vacuum for 30 min to afford a cadmium precursor solution; 5 ml of the prepared PbS QDs suspended in toluene was bubbled with argon for 10 min and then injected into the cadmium precursor solution. The reaction flask was quenched with 5 ml cold hexane after the growth reaction was conducted at 100 °C for 60 min. The PbS/CdS QDs were precipitated with ethanol and then redispersed in hexane.

Surface modification of PbS/CdS QDs with P^3 coating. Chloroform solution (0.5 ml) containing 10 mg PMH was mixed with 2 mg QDs dispersed in 0.5 ml cyclohexane. After overnight stirring, the organic solvent was evaporated for 30 min by a rotary evaporator. The excess residual was heated at 60 °C for 3 h to fully remove the remaining organic solvent. Afterwards, 1 ml 4-(dimethylamino) pyridine (10 mg) aqueous solution was added, and the flask was placed in a sonication bath for 10 min to allow the QDs to be fully transferred to the water phase. Furthermore, the QD solution was centrifuged at 50,000 r.p.m for 2.5 h. The precipitates were resuspended in 0.5 ml MES (10 mM, pH = 8.5) followed by the addition of 1.5 mg 8Arm-PEG-NH_2•HCl (average molecular weight = 40 kDa) in 1 ml MES (pH = 8.5) and 1 mg EDC. The solution reacted for 3 h on an orbital shaker. The remaining carboxylic groups were quenched by adding 5 mg tris-base and 2.5 mg EDC to the above solution. After the reaction completed, the product was dialysed against water for 12 h (300 kDa) to completely remove any by-products. The purification was completed by washing the supernatant with a centrifuge filter tube (100 kDa) and the concentrated sample inside the filter was dispersed in 0.5 ml MES (10 mM, pH = 8.5) solution. PAA (0.5 mg; average molecular weight = 1.8 kDa) in 1 ml MES (10 mM, pH = 8.5), together with 1 mg EDC, was added and the QD solution was allowed to react for 1 h. Any large floccules were removed by the centrifugation of solution at 4,400 r.p.m for 30 min, followed by the washing of supernatant by a centrifuge tube (100 kDa) four times. The as-prepared QD@PMH-8Arm-PEG-PAA was redispersed in 0.5 ml MES solution for final layer coating. As such, the above QD@PMH-8Arm-PEG-PAA was mixed with 0.5 mg mPEG-NH_2 (average molecular weight = 5 kDa), and 0.1 mg 8Arm-PEG-NH_2•HCl (average molecular weight = 40 kDa) in 1 ml MES solution (10 mM, pH = 8.5). After adding of 1 mg EDC, and the solution was allowed to react for 3 h; 5 mg tris-base and 2.5 mg EDC were then added into the above solution and left to react for another 3 h. The reaction product was centrifuged at 4,400 r.p.m for 30 min to remove potential large aggregates, the supernatant was then washed by a centrifuge filter (100 kDa) four times. The final QD@PMH-8Arm-PEG-PAA-mixed PEG were dispersed in 500 µl 1× PBS solution for further use.

The quantum yield of P^3-QDc was ~1.0% at 808 nm excitation, lower but close to the quantum yield of P^3-QDb (2.6%)[12] in aqueous solution measured by an integrating sphere as described previously[14].

Conjugation of antibodies on QDs. *aMECA-79-QDc.* MECA-79 antibody (100 µg) was washed by centrifuge filter (10 kDa) four times to remove sodium azide. P^3-QDc (0.25 mg) dispersed in 50 µl 1× PBS solution, MECA-79 antibody (100 µg), EDC (0.6 mg) and 450 µl MES solution (10 mM, pH = 8.0) was mixed and shaken for 3 h. The solution was first centrifuged at 4,400 r.p.m for 30 min to remove potential large floccules. The supernatant was washed by centrifuge filter (10 kDa) four times and then dispersed in 200 µl 1× PBS solution for further intravenous injection.

aCD3-QDc. P^3-QDc (0.25 mg) dispersed in 50 µl 1× PBS solution, CD3 antibody (200 µg), EDC (0.6 mg) and 450 µl MES solution (10 mM, pH = 8.0) were mixed and shaken for 3 h. The solution was first centrifuged at 4,400 r.p.m for 30 min to remove potential large floccules. The supernatant was washed by centrifuge filter (10 kDa) four times and then dispersed in 50 µl 1× PBS solution for further subcutaneous injection.

aCD169-QDa. QDa (0.025 mg) dispersed in 50 µl 1× PBS solution, CD169 antibody (50 µg), EDC (0.6 mg) and 450 µl MES solution (10 mM, pH = 8.0) were mixed and shaken for 3 h. The solution was first centrifuged at 4,400 r.p.m for 30 min to remove potential large floccules. The supernatant was washed by centrifuge filter (10 kDa) four times and then dispersed in 50 µl 1× PBS solution for further subcutaneous injection.

NIR-II confocal microscope. A laser beam with a wavelength of 808 nm, 1,319 nm, 1,540 nm or 1,650 nm was reflected by a galvo mirror (GVS002, Thorlabs) into a Plössl scan lens (constructed from two achromatic doublets, L3, L4, AC508-150-C, Thorlabs), a Plössl tube lens (constructed from two achromatic doublets, L1, L2, AC508-300-C, Thorlabs) and then focused by an objective into a sample (Supplementary Fig. 3). The fluorescence signal was collected by the same objective, tube lens and scan lens. After descanned by the galvo mirror and resized by two achromatic doublets (L5, AC254-100-C and L6, AC508-150-C), the fluorescence light was focused into three single-mode fibres (P1-SMF28E-FC-5, Thorlabs) by achromatic doublets (L7-L9, AC254-030-C, Thorlabs) after being filtered by selected emission filters. The single-mode fibre (~10 µm mode field diameter) then transmitted the fluorescence to NIR-IIb or NIR-IIc SNSPDs. The datasheet of P1-SMF28E-FC-5 only gives attenuation data at 1,260–1,625 nm. We examined the attenuation of this single-mode fibre at 1,000–2,000 nm by measuring the emission spectrum of a mixture of three PbS/CdS QDs (emission peaks at 1,100 nm, 1,340 nm, 1,650 nm and 1,880 nm) using a spectrometer connected to a one-dimensional extended InGaAs camera (Princeton Instruments) or SNSPDs coupled with the single-mode fibre. The experimental results show that the fibre-coupled SNSPD has some attenuation at wavelengths longer than 1,678 nm, but the attenuation degree is still acceptable for 1,200–2,000 nm imaging (Supplementary Fig. 4).

For confocal microscopy with PMT (H12397-75, Hamamatsu), a multimode fibre (M122L01, Thorlabs) with a core diameter of 200 µm was necessary to afford sufficient fluorescence signal detectable by the PMT (Supplementary Fig. 11a). We also investigated the fibre effect by imaging blood vessels in mouse stomachs in the NIR-IIb window ex vivo. We found that the 200 µm multimode fibre in fact afforded a much higher detection signal than the small 10 µm single-mode fibre (P1-SMF28E-FC-5, Tholrabs) (Supplementary Fig. 11b–f). We also compared the sensitivity of PMT and SNSPD by NIR-IIb imaging of a 50 µm capillary embedded in 5% intralipid solution at 1,319 nm excitation and using a ~10 µm core single-mode fibre as a pin-hole. We found that the SNSPD allowed a 2.6 mm imaging depth (Fig. 2a), whereas no signal was detected at an intralipid layer depth of 1.3 mm using PMT (Supplementary Fig. 11a), suggesting the superior sensitivity of SNSPD over PMT.

The galvo mirror, SNSPD and a motorized translation stage (M-VP-25XL, Newport) were synchronized by an acquisition card (NI PCIe-6374) through Labview. This acquisition card also worked as a photon counter to count the TTL signal generated by SNSPD when photons were detected (Supplementary Fig. 3). We used 5× (NA = 0.12, Leica N Plan), 10× (NA = 0.25, Olympus ULWD MIRPlan), 20× (NA = 0.4, Olympus ULWD MIRPlan), 20× (NA = 0.75, Nikon Plan APO), 25× (NA = 1.05, Olympus XLPLN25XWMP2) and 100× objectives (NA = 0.8, Olympus ULWD MIRPlan) in this work. We used D_2O as the immersion liquid for the 25× objective (NA = 1.05) to minimize the absorption by this immersion layer.

For NIR-IIb imaging, longpass filters with a cut-on wavelength of 1,500 nm (FELH1500, Thorlabs) or 1,580 nm (BLP01-1550R-25) and a bandpass filter (BBP-1,530–1,730 nm, Spectrogon) were used to generate imaging windows of ~1,500–1,700 nm or 1,580–1,700 nm, respectively. For NIR-IIc imaging with 1,540 nm excitation, two bandpass filters (FB1750-500 with a transmittance window in 1,500–2,000 nm and FB2000-500 with a transmittance window in 1,750–2,250 nm, Thorlabs) were combined for 1,750–2,000 nm fluorescence collection. For NIR-IIc imaging with 1,650 nm excitation, a bandpass filter (FB1900-200 with a transmittance window in 1,800–2,000 nm was used. A short-pass filter with a cut-off wavelength of 1,600 nm (nos 84–656, Edmund optics) was used to filter 1,540 nm laser. For confocal microscopy with 1,000–1,400 nm emission and 808 nm excitation, a longpass dichroic mirror with cut-on wavelength at 980 nm was used (Di02-R980-25×36, Semrock). For NIR-IIb and NIR-IIc confocal microscopy, longpass dichroic mirrors with cut-on wavelengths at 1,500 nm and 1,800 nm were used, respectively (DMLP1500R, DMLP1800R, Thorlabs).

Resolution analysis. We analysed the spatial resolution of confocal microscopy with SNSPD by experimental measurements and modelling (see Supplementary Note 3). To estimate the system's best resolution without worsening scattering, we imaged 300 nm polystyrene beads containing a NIR-II organic dye[20] with different objectives. The nanoparticles were deposited on a coverslip. A fluorescence emission of >1,100 nm was collected at 658 nm excitation. The experimental measured FWHM of nanoparticles were consistent with the FWHM of a theoretically calculated PSF along the lateral and vertical directions (Supplementary Fig. 12). When a 25× objective (numerical aperture, NA = 1.05) was used, FWHMs of ~0.4 μm and ~1 μm can be achieved in the lateral and vertical directions, respectively. The agreement of experimental data and modelling suggested validity of the analysis for imaging with the organic dyed beads emitting in the 1,000–1,300 nm range. Due to the lack of beads emitting in NIR-IIc, we only performed modelling and calculated the PSF of confocal microscope in the NIR-IIc window as a function of the pin-hole diameter. When a 25× objective (NA = 1.05) and a 1,650 nm laser was used, and the fluorescence was collected in NIR-IIc window, the calculated PSF shows FWHMs of ~0.83 μm and ~1.82 μm in the lateral and vertical direction, respectively (Supplementary Fig. 13). To estimate the resolution of NIR-IIc confocal microscopy (excitation = 1,650 nm; emission = 1,800–2,000 nm) affected by scattering, we imaged mouse brain with circulating P^3-QDc in blood vessels after sacrificing the mouse, fixation and immersion in 80% glycerol. The measured FWHM of blood vessels was analysed. The FWHMs of small vessels were ~2.0 ± 0.45 μm and 7.1 ± 0.75 μm in the lateral and axial directions, respectively, at depths between 100 μm and 1,500 μm in the mouse brain (Supplementary Fig. 14). These corresponded to the lateral and axial resolution limits[1] of NIR-IIc confocal imaging.

Data processing. The raw data of confocal microscopy was processed by a Gaussian filter in ImageJ (1.53c). Three-dimensional rendering and multicolour fluorescence image merging were also performed in ImageJ or ImarisViewer 9.6.0 (Oxford Instruments). The FWHM was measured in Origin 9.0. The standard deviation and mean were calculated by Origin 9.0. The PSF was calculated in Matlab (R2019b).

Mouse handling. All procedures performed on the mice were approved by Stanford University's Institutional Animal Care and Use Committee. All experiments were performed according to the National Institutes of Health Guide for the Care and Use of Laboratory Animals. The laboratory animal care program at Stanford is accredited by the Association for the Assessment and Accreditation of Laboratory Animal Care. BALB/c female mice were purchased from Charles River. Through this work, we used three-week-old BALB/c mice (weight ≈ 7 g). The mice were housed on a 12 h:12 h light:dark cycle (temperature = 20–25 °C; humidity = 50–65%) in Stanford University's Veterinary Service Center and fed with food and water ad libitum as appropriate. Mice were shaved using hair remover lotion (Nair, Softening Baby Oil). Mice were randomly selected from cages for all experiments. During in vivo imaging, all mice were anaesthetised by a rodent anaesthesia machine with 2 l min^{-1} O_2 gas mixed with 3% isoflurane.

In vivo wide-field NIR-II fluorescence imaging. The NIR-II wide-field fluorescence images were recorded by a two-dimensional water cooled InGaAs camera (Ninox640, Raptor Photonics) working at −21 °C. For two-plex imaging, aMECA-79-QDc and p-FE, or aCD3-QDc and aCD169-QDa, were excited by an 808 nm continuous-wave diode laser. The fluorescence of aMECA-79-QDc and p-FE was collected at 1,500–1,700 nm and 1,200–1,400 nm, respectively. The actual excitation intensity was ~70 mW cm^{-2}. The fluorescence signal was collected by two achromatic lenses to the camera after filtered by corresponding long- and short-pass filters.

In vivo NIR-IIc confocal microscopy of mouse head. To image the blood vessels distribution in mouse head non-invasively (Fig. 3), a three-week-old BALB/c mouse was intravenously injected with 200 μl NIR-IIb P^3-QDb (OD = 5 at 808 nm) and 200 μl NIR-IIc P^3-QDc (OD = 5 at 808 nm) sequentially through the tail vein. NIR-IIb and NIR-IIc confocal microscopy was performed 30 min after injection with a 25× objective (NA = 1.05). Detailed experimental conditions are summarized in Supplementary Table 1.

In vivo NIR-IIc confocal microscopy of HEVs in iLNs. For two-colour confocal microscopy of HEVs in iLNs and blood vessels around the iLNs, a three-week-old BALB/c mouse was first injected with 200 μl aMECA-79-QDc (OD = 0.75 at 808 nm) intravenously; 24 h later, 200 μl p-FE (OD = 5 at 808 nm) was injected into the tail vein to label the blood vessels. Two-colour NIR-II confocal microscopy was performed 10 min after injection. Detailed experimental conditions are summarized in Supplementary Table 1.

In vivo and ex vivo NIR-IIc confocal microscopy of immune cells in iLNs. For two-colour confocal microscopy of CD169+ macrophages and CD3+ T cells in iLNs, a three-week-old BALB/c mouse was subcutaneously injected with 50 μl aCD169-QDa (OD = 0.3 at 808 nm) and 50 μl aCD3-QDc (OD = 3 at 808 nm). Two-colour NIR-II confocal microscopy was performed 24 h after injection. The scan step, dwell time, excitation wavelength filters and laser powers are summarized in Supplementary Table 1.

After in vivo confocal microscopy, the mouse was euthanized under anaesthesia. The iLNs were taken out and fixed with 10% neutral-buffered formalin at room temperature for 30 min. They were then washed by 1X PBS buffer three times and labelled by DRAQ7 for 3 h. After being washed in 1× PBS buffer three times, the iLNs were preserved in glycerol at 4 °C for ex vivo imaging.

Reporting summary. Further information on research design is available in the Nature Research Reporting Summary linked to this article.

Data availability

Source data are provided with this paper. All data that support the findings of this study are presented in the main text and the Supplementary Information. Source Data are provided with this paper.

Acknowledgements

This study was supported by the National Institutes of Health (NIH DP1-NS-105737, H.D.). We thank K. Taylor from JASCO who helped measuring the UV–vis–NIR absorbance spectrum of water using their V-770 Spectrophotometer. F.R. thanks the Fonds de recherche du Québec—Nature et technologies (FRQNT) for funding (F.R.). Single Quantum acknowledges support from the EIC SME Phase 2 project SQP (grant no. 848827 to R.G., J.W.L., A.F. and J.Q-.D.).

Author contributions

H.D. and F.W. conceived and designed the experiments. H.D. and F.W. designed the optical system. F.W. set up the optical system. F.W., F.R. and Z.M. performed the experiments. F.R. synthesized the PbS/CdS QD. R.G., I.E.Z., J.W.N.L., A.F. and J.Q-.D. developed the SNSPD optimized in a 1,550–2,000 nm window. F.W., F.R., Z.M., L.Q., C.X., A.B., J.L. and H.D. analysed the data. F.W. and H.D. wrote the manuscript. All authors contributed to the general discussion and revision of the manuscript.

Competing interests

The following authors were employed by Single Quantum and may profit financially: R.G., J.W.L., A.F. and J.Q.D.

Additional information

Supplementary information The online version contains supplementary material available at https://doi.org/10.1038/s41565-022-01130-3.

Correspondence and requests for materials should be addressed to Hongjie Dai.

Peer review information *Nature Nanotechnology* thanks Eva Sevick-Muraca, Wei Zheng and the other, anonymous, reviewer(s) for their contribution to the peer review of this work.

Reprints and permissions information is available at www.nature.com/reprints.

Corresponding author(s): Hongjie Dai

Last updated by author(s): Mar 24, 2022

Reporting Summary

Nature Portfolio wishes to improve the reproducibility of the work that we publish. This form provides structure for consistency and transparency in reporting. For further information on Nature Portfolio policies, see our Editorial Policies and the Editorial Policy Checklist.

Statistics

For all statistical analyses, confirm that the following items are present in the figure legend, table legend, main text, or Methods section.

n/a	Confirmed	
☐	☒	The exact sample size (*n*) for each experimental group/condition, given as a discrete number and unit of measurement
☐	☒	A statement on whether measurements were taken from distinct samples or whether the same sample was measured repeatedly
☒	☐	The statistical test(s) used AND whether they are one- or two-sided *Only common tests should be described solely by name; describe more complex techniques in the Methods section.*
☒	☐	A description of all covariates tested
☒	☐	A description of any assumptions or corrections, such as tests of normality and adjustment for multiple comparisons
☐	☒	A full description of the statistical parameters including central tendency (e.g. means) or other basic estimates (e.g. regression coefficient) AND variation (e.g. standard deviation) or associated estimates of uncertainty (e.g. confidence intervals)
☒	☐	For null hypothesis testing, the test statistic (e.g. *F*, *t*, *r*) with confidence intervals, effect sizes, degrees of freedom and *P* value noted *Give P values as exact values whenever suitable.*
☒	☐	For Bayesian analysis, information on the choice of priors and Markov chain Monte Carlo settings
☒	☐	For hierarchical and complex designs, identification of the appropriate level for tests and full reporting of outcomes
☒	☐	Estimates of effect sizes (e.g. Cohen's *d*, Pearson's *r*), indicating how they were calculated

Our web collection on statistics for biologists contains articles on many of the points above.

Software and code

Policy information about availability of computer code

Data collection	LabView2014 was used to synchronously control the laser power, photon counting , galvo mirror and motorized stage.
Data analysis	The raw data of confocal microscopy was processed by a Gaussian filter in ImageJ (1.53c). 3D rendering and multi-color fluorescence image merging were also performed in ImageJ (1.53c) or ImarisViewer 9.6.0 (Oxford Instruments). The FWHM was measured in Origin 9.0. The standard deviation and mean were calculated by Origin 9.0. The PSF was calculated in Matlab (R2019b).

For manuscripts utilizing custom algorithms or software that are central to the research but not yet described in published literature, software must be made available to editors and reviewers. We strongly encourage code deposition in a community repository (e.g. GitHub). See the Nature Portfolio guidelines for submitting code & software for further information.

Data

Policy information about availability of data

All manuscripts must include a data availability statement. This statement should provide the following information, where applicable:

- Accession codes, unique identifiers, or web links for publicly available datasets
- A description of any restrictions on data availability
- For clinical datasets or third party data, please ensure that the statement adheres to our policy

Source data are provided with this paper. All data that support the findings of this study are presented in the main text and the Supplementary Information.

Field-specific reporting

Please select the one below that is the best fit for your research. If you are not sure, read the appropriate sections before making your selection.

☒ Life sciences ☐ Behavioural & social sciences ☐ Ecological, evolutionary & environmental sciences

For a reference copy of the document with all sections, see nature.com/documents/nr-reporting-summary-flat.pdf

Life sciences study design

All studies must disclose on these points even when the disclosure is negative.

Sample size	Sample sizes were provided in the figure legends for each experiment. Sample sizes were chosen on the basis of previous publications (Nature Methods 2017, 14, 388–390; Nature Methods, 2018, 15,789–792; Nature Nanotechnology 2009, 4, 773–780; Nature Methods 2019, 16, 545–552).
Data exclusions	No data were excluded from the analyses.
Replication	All experiments were carried out at least 3 times successfully.
Randomization	Mice were randomly selected from cages, divided into groups for the studies.
Blinding	The investigators were blinded to group allocation during data collection and/or analysis

Reporting for specific materials, systems and methods

We require information from authors about some types of materials, experimental systems and methods used in many studies. Here, indicate whether each material, system or method listed is relevant to your study. If you are not sure if a list item applies to your research, read the appropriate section before selecting a response.

Materials & experimental systems

n/a	Involved in the study	
☐	☒	Antibodies
☒	☐	Eukaryotic cell lines
☒	☐	Palaeontology and archaeology
☐	☒	Animals and other organisms
☒	☐	Human research participants
☒	☐	Clinical data
☒	☐	Dual use research of concern

Methods

n/a	Involved in the study	
☒	☐	ChIP-seq
☒	☐	Flow cytometry
☒	☐	MRI-based neuroimaging

Antibodies

Antibodies used	1. Purified anti-mouse/human PNAd antibody (BioLegend; Clone: MECA-79; Cat. #.: 120802; Dilution: 100 ug/ 200 uL) 2. Purified anti-mouse CD169 antibody (BioLegend; Clone: 3D6.112; Cat. #.: 142402; Dilution: 50 ug/ 50 uL) 3. DRAQ7 (BioLegend; Cat. #.: 424001; Dilution: 1:100) 4. Anti-mouse CD3 antibody (BioXCell; Clone: KT3; Cat. #.: BE0261; Dilution: 200 ug/ 200 uL) The conjugation procedure can be found in Methods.
Validation	The antibodies used in this study were commercially available. There are publications using these antibodies. For purified anti-mouse/human PNAd antibody (Clone: MECA-79): (1) Thomas SN, et al. 2012. J. Immunol. 189:2181 (2) Hirakawa J, et al. 2010. J. Biol. Chem. 285:40864 For purified anti-mouse CD169 antibody (Clone: 3D6.112) : (1) Barral P, et al. 2010. Nat. Immunol. 11:303 (2) Klass M, et al. 2012. J. Immunol. 189:2414 For DRAQ7 (# 424001) (1) Pavesi A, et al. 2016. Sci Rep. 6: 26584 (2) Garvey C, et al. 2016. Sci Rep. 6:29752 For Anti-mouse CD3 antibody (Clone: KT3) (1) Reuter, A., et al. (2015). J Immunol 194(6): 2696-2705 (2) Sathe, P., et al. (2014). Immunity 41(1): 104-115.

Animals and other organisms

Policy information about studies involving animals; ARRIVE guidelines recommended for reporting animal research

Laboratory animals	3-week-old BALB/c female mice were purchased from Charles River. The animals were housed on a 12 h: 12 h light: dark cycle (temperature: 20–25 °C, humidity: 50–65 %) in the Stanford University’s Veterinary Service Center (VSC), and fed with food and water ad libitum as appropriate.
Wild animals	No wild animals were used in this study.
Field-collected samples	No field-collected samples were used.
Ethics oversight	All procedures performed on the mice were approved by Stanford University's Institutional Animal Care and Use Committee (IACUC). All experiments were performed according to the National Institutes of Health Guide for the Care and Use of Laboratory Animals. The laboratory animal care program at Stanford is accredited by the Association for the Assessment and Accreditation of Laboratory Animal Care (AAALAC).

Note that full information on the approval of the study protocol must also be provided in the manuscript.